

Quantifying The Complex Spatiotemporal Chaos of Cardiac Fibrillation in Ionic Models Across Parameter Regimes

Xiaodong An,¹ Mikael Toye,¹ and Flavio H. Fenton¹

School of Physics, Georgia Institute of Technology, Atlanta, Georgia 30332, USA

(Dated: August 21, 2025)

Quantifying the complexity of cardiac systems is fundamental to understanding the onset of rhythm disorders, from mild arrhythmias to life-threatening fibrillation. In this work, we investigate how chaos shows up and evolves in simplified cardiac models by calculating the Lyapunov exponent (LE) across different parameter sets. We show that both temporal and spatial LE estimators can be effectively applied to action potential duration (APD) data, even without full access to state variables. Specifically, the spatial-temporal algorithm and Wolf’s algorithm are used in quantifying the complexity, with experiments demonstrating their distinct behaviors on various single-spiral patterns. We also identify the minimum data length and sampling density necessary to achieve robust and accurate estimation. Overall, our results suggest that these APD-based methods can be applied not only to simulation data but also to future clinical or experimental data, particularly when observations are limited, such as when only APD data are available for analysis.

Irregular cardiac activities, such as arrhythmia and fibrillation, are often linked to chaotic electrical activity in the heart. Measuring this chaos typically requires full access to state variables that are hard to obtain in real-world settings. In this study, we show that a simple and commonly measured signal, APD, can be used to reveal key features of cardiac instability, offering a practical tool for both experimental and clinical applications.

I. INTRODUCTION

In recent years, there has been growing interest in understanding and characterizing spatiotemporal chaos in cardiac tissue^{1–3}. Spatiotemporal chaos can emerge in cardiac tissue due to its inherent nonlinear dynamics, causing dangerous cardiac rhythm disorders such as fibrillation^{4–8}. Being able to quantify the chaos could deepen our understanding of cardiac instability and guide early diagnosis and treatment strategies^{9,10}. While LE is widely used as an indicator for chaos, most studies focus on temporal LEs derived from full voltage data^{11,12}. In practical scenarios, however, only partial observations (short recordings), including APD from optical mapping or ECG, may be available. Also, spatial aspects of dynamics are often overlooked in conventional approaches^{13–16}. This highlights the need for resource-efficient methods that can also take spatial information into account.

This study aims to quantify the spatiotemporal chaos and explore whether APD sequences in time and space from simulations of ionic cardiac cell models can be used to quantify the underlying dynamics of the system, and

provide a measurement for chaos as parameters of the models are varied. We apply both temporal (Wolf’s Algorithm¹²) and spatial-temporal LE¹⁷ (SLE) methods to data obtained from ionic models, including the 3V-SIM model⁴ and O’Hara-Virág-Varró-Rudy (OVVR) human model¹⁸, with different dynamics, under various parameter sets. Through a systematic evaluation on several single-spiral wave patterns, we find that the two methods respond differently depending on whether the chaos originates from spiral tip drifting or from shape deformation. By comparing the LE results with parameter transitions, we can establish a link between chaotic transitions and model gating parameters.

In addition, we conduct a series of experiments to identify how temporal length and spatial sampling resolution affect the stability and accuracy of chaos quantification. The temporal LE requires longer sequences but offers higher precision, while the spatial LE converges faster with fewer data points. These findings are useful for real-world applications, especially when dealing with noisy or short-duration experimental recordings. Our goal is to bridge theoretical modeling with practical application by showing that LE-based chaos estimation could be extended to experimental and machine learning pipelines using APD sequences alone.

II. METHODS

LE¹⁹ is a quantitative measure of the divergence rate for nearby trajectories, implying the stability of a nonlinear system, spatially or temporally. LEs are defined as:

$$\lambda(\mathbf{X}(0)) = \lim_{t \rightarrow \infty} \frac{1}{t} \ln \frac{\|J^t(\mathbf{X}(0)) \delta \mathbf{X}(0)\|}{\|\delta \mathbf{X}(0)\|}, \quad (1)$$

where $J^t(\mathbf{X}(0)) = \prod_{t'=1}^t J^{t'}(\mathbf{X}(0))$ is the Jacobian matrix. However, in practical cases where the Jacobian matrix is impossible to obtain (too many state variables or indeterminate original partial differential equations (PDEs) of the system), people have developed several data-driven algorithms to estimate LEs, including temporal and spatial LEs. Here we utilized Wolf's algorithm¹² for temporal LE estimation and the spatio-temporal algorithm by Solé and Bascompte¹⁷ for spatial LE estimation.

A. Temporal LE

Wolf's algorithm¹² for calculating LE is widely utilized to quantify the rate at which nearby trajectories in a dynamical system diverge. Instead of relying solely on one trajectory with initial point $\mathbf{X}(0)$ as shown in Eq. 1, the algorithm selects multiple trajectories in a temporal data set. This approach mitigates the risk of selecting a non-representative trajectory, such as one located on a periodic orbit or within atypical attractors, thereby ensuring a more robust and accurate estimation of the LE. However, the method does not incorporate spatial information if the points are correlated, such as in the case of cardiac tissue by diffusion.

For a phase space Γ (or reconstructed phase space $\Gamma^{m,\tau}$ that is diffeomorphic to the true phase space Γ)²⁰ with total time step N , we have the following:

$$\Gamma^{m,\tau} \cong \Gamma = \left\{ \mathbf{X}_i = \begin{pmatrix} u_i, v_i, w_i \end{pmatrix} \right\}, i = 1, \dots, N. \quad (2)$$

For a point in the phase space, find a nearby point (a neighbor) that lies on a different trajectory. This neighbor should be close in phase space (both their magnitude and direction) but not necessarily in time to avoid correlations between temporally adjacent trajectories.

Specifically, a point \mathbf{X}_i where $i \approx \frac{N}{2}$ in the first iteration and $i = i'$ otherwise, is chosen, then by iterating through Γ , we find its nearest neighbor \mathbf{X}_j by calculating the Euclidean distance:

$$\arg \min_j \|\mathbf{X}_i - \mathbf{X}_j\| = \arg \min_j L_i < \varepsilon, \quad (3)$$

where

- $j \neq i$.

- $\frac{\mathbf{X}_i \mathbf{X}_j}{\|\mathbf{X}_i\| \|\mathbf{X}_j\|} < \theta$.
- $\theta = \frac{\pi}{9}$ is the maximum initial angular distance.
- ε is the maximum initial separation.

If the algorithm cannot find a close enough pair whose Euclidean distance is smaller than ε , then ε is increased.

Then L_i is evolved by one time step each until:

$$\|\mathbf{X}_{i'} - \mathbf{X}_{j'}\| = L_{i'} > \varepsilon \text{ or } i' \geq N \text{ or } j' \geq N, \quad (4)$$

where ε should be chosen sufficiently large to ensure the two neighbors exhibit chaotic behavior.

If the evolved distance exceeds ε , repeat Eq. 3 and Eq. 4. If not, break the loop and continue to Eq. 5.

During the loop, record all the $\frac{L_{i'}}{L_i}$, the i in first loop as i_0 and the i' in last loop as i_f . Finally, the temporal LE is²¹:

$$\lambda_t \equiv \frac{1}{i_f - i_0} \sum_{\text{All Loops}} \log_2 \frac{L_{i'}}{L_i}, \quad (5)$$

with every pixel recorded in the 2D simulated tissue, there is a time series data that contains a temporal LE, so on average, it becomes:

$$\bar{\lambda}_t = \frac{1}{\# \text{ of Pixels}} \sum_{\text{All Pixels}} \frac{1}{i_f - i_0} \sum_{\text{All Loops}} \log_2 \frac{L_{i'}}{L_i}, \quad (6)$$

B. Spatial LE

Classical LE algorithms like Wolf's Algorithm mainly focus on temporal chaos. While SLE can quantify how local perturbations evolve and spread through space over time. This provides a more comprehensive understanding of the global dynamics of the system by capturing both temporal and spatial variations and instabilities.

Now, a 2D map $\Lambda^2(L)$ is defined as:

$$\Lambda^2(L) = \{\mathbf{k} = (\alpha, \beta) \mid 1 \leq \alpha, \beta \leq L\}, \quad (7)$$

where:

- L is the length of map.
- \mathbf{k} is the pixel in map.
- α, β is the x, y coordinate of the pixel \mathbf{k} .

It is easy to see that:

$$\Gamma^{m,\tau}(\Lambda^2) \cong \Gamma(\Lambda^2) = \bigcup_{\mathbf{k} \in \Lambda} \Gamma(\mathbf{k}). \quad (8)$$

For each $\mathbf{X}_i(\mathbf{k}) \in \Gamma(\mathbf{k}), \forall \mathbf{k} \in \Lambda^2$, we search its neighbor $\mathbf{h} \in \Lambda^2, \mathbf{h} \neq \mathbf{k}$ such that the following condition holds:

$$\|\mathbf{X}_i(\mathbf{k}) - \mathbf{X}_i(\mathbf{h})\| < \varepsilon, \quad (9)$$

where ε is the maximum initial separation.

Then evolve the pair to one more step further, which is to calculate:

$$\|\mathbf{X}_{i+1}(\mathbf{k}) - \mathbf{X}_{i+1}(\mathbf{h})\|. \quad (10)$$

Finally, SLE is defined as:

$$\lambda_s(m, \tau) = \frac{1}{N_{pair}} \sum_{i=1}^{N-1} \sum_{\langle \mathbf{k}, \mathbf{h} \rangle} \log_2 \left(\frac{\|\mathbf{X}_{i+1}(\mathbf{k}) - \mathbf{X}_{i+1}(\mathbf{h})\|}{\|\mathbf{X}_i(\mathbf{k}) - \mathbf{X}_i(\mathbf{h})\|} \right). \quad (11)$$

C. Phase Space Reconstruction

Rather than solely quantifying the original phase space, we also investigated the scenario involving a restricted observation of state variables. We applied phase space reconstruction on this data, which is based on Takens' Embedding Theorem²⁰. "For Takens' Embedding, two variables need to be determined": embedded dimension m and lagging τ . The lagging τ is typically selected first, followed by the embedding dimension m .

Embeddings with the same m but different τ are equivalent in the mathematical sense for noise-free data²². Therefore, for the purposes of this research, where simulations are conducted without the influence of noise, a simple choice of $\tau = 1$ is sufficient.

The embedding dimension refers to the number of delayed elements for the time series $\gamma = \{x_i\}$ used to construct the embedded vector \mathbf{X}_i . To reconstruct phase space successfully, the sufficient condition would be^{20, 23}:

$$m > 2d, m > 2d_c, \quad (12)$$

where: d is the phase space dimension and d_c is the box-counting dimension of strange attractors.

However, Sugihara et al.²⁴ state that the embedded dimension can be:

$$m \approx d, \quad (13)$$

where they successfully reconstructs the Lorenz system ($d = 3$) with $m = 3$ by plotting the reconstructed phase space and original phase space and showing that they are geometrically same.

Therefore, we may conclude that m in $[d, 2d]$ or $[d, 2d_c]$ could be appropriate, with its exact minimum value depending on the nature of the dataset being analyzed. Several methods exist for determining an optimal embedding dimension, including the False Nearest Neighbor (FNN) method²⁵, the Characteristic Decay Rate¹⁷, the Fuzzy Clustering²⁶, the Fill-Factor method²⁷, the Average Integral Local Deformation (AILD) method²⁷, and so on. A comprehensive summary of these algorithms can be found in Jiang and Adeli²⁶. Most of the approaches above rely on the fact that, once m exceeds the minimum embedding dimension, the reconstructed phase space would be geometrically the same as the true phase space. Furthermore, a reasonable data length required to determine the embedded dimension is at least 10^m ²⁸. Accordingly, the success of those algorithms requires the dynamical system to behave in a low dimension with sufficiently long data as input.

Now, in this paper, we apply the FNN method, with $\tau = 1$, we first initialize different embedded dimensions $\{m\}$.

For every embedded vector with a certain m :

$$\mathbf{X}_i^{m, \tau=1} = \{x_i, x_{i+\tau}, x_{i+2\tau}, \dots, x_{i+(m-1)\tau}\}, \quad (14)$$

$$i = 1, 2, \dots, N - m\tau + \tau,$$

find its nearest neighbor \mathbf{X}_j^m such that $j = \arg \min_j \|\mathbf{X}_i^m - \mathbf{X}_j^m\| = \arg \min_j R_i^m$.

We get $R_i^{m+1} = \|\mathbf{X}_i^{m+1} - \mathbf{X}_j^{m+1}\|$. Now i, j will be identified as a pair of false neighbors if $|R_i^m - R_i^{m+1}| \gg 0$.

Specifically, if the ratio:

$$R(i, m) = \sqrt{\frac{(R_i^m)^2 - (R_i^{m+1})^2}{(R_i^m)^2}} \quad (15)$$

is bigger than a pre-defined value $R_0 = 10$, we call $\{i, j\}$ a pair of false neighbors or point i has a false neighbor j .

Now, if at a certain embedded dimension m_0 , the percentage of false nearest neighbors $\frac{\text{false pairs of neighbors}}{\text{total pairs of neighbors}}$ does not decrease, we could identify m_0 as the correct dimension.

D. 3V-SIM Model

3V-SIM (Simplified Ionic Model) model also known as the Fenton-Karma Model was developed in 1990s and can quantitatively reproduce the APD of a cell as a function of its Diastolic Interval, APD vs DI curves (restitution curves) are used to quantitatively determine the dynamics of cardiac cells as their period of excitation changes⁴. This model's aims are to provide a simplified solution to simulate the electrical activity in cardiac tissue. Moreover, it balances the computational cost and physiological accuracy, making it quite useful in large-scale simulations with studies of arrhythmic behaviors in the heart.

Specifically, 3V-SIM model has three trans-membrane currents: fast inward (I_{fi} or Na^+), slow inward (I_{si} or Ca^{2+}), and slow outward current (I_{so} or K^+). Now, even with the names Na^+ , Ca^{2+} , and K^+ , it does not mean they represent those measured currents but only their activation and inactivation characteristics⁴. What's more, three state variables are defined as membrane voltage (u), and gate variables (v, w) where the latter two control the inactivation and reactivation of currents (similar models but with four state variables are defined in^{29,30}). During the whole activation-inactivation process as shown in Fig. 1, I_{fi} is responsible for the depolarization (upstroke part ①) of membrane voltage, which is controlled by gate v , I_{so} is responsible for the repolarization of membrane voltage (part ③) and I_{si} is responsible for maintaining the plateau (part ②) after depolarization, which is controlled by gate w .

By tuning this model's parameters, there are different sets where the model could replicate restitution curves from other more complex models such as the Beeler-Reuter (BR) model³¹, modified forms of the Beeler-Reuter (MBR) model³¹, Luo-Rudy-I (MLR-I) model³², and also optical mapping of the epicardium (outermost heart layer) in the left ventricle of a pig⁴. This model has been also used in⁵ to investigate various different mechanisms for spiral wave breakups.

The 3V-Sim model equations are given by⁵:

$$\begin{aligned}\partial_t u(x, t) &= D \nabla^2 u - (I_{fi}(u, v) + I_{so}(u) + I_{si}(v, w)) / C_m \\ \partial_t v(x, t) &= (1 - p)(1 - v) / \tau_v^-(u) - pv / \tau_v^+ \\ \partial_t w(x, t) &= (1 - p)(1 - w) / \tau_w^- - pw / \tau_w^+\end{aligned}\quad (16)$$

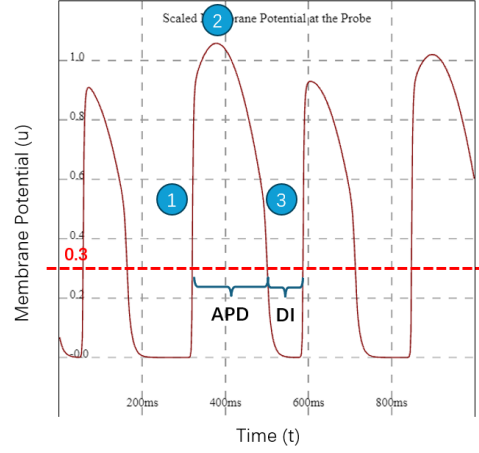


Figure 1. Membrane potential by 3V SIM Model

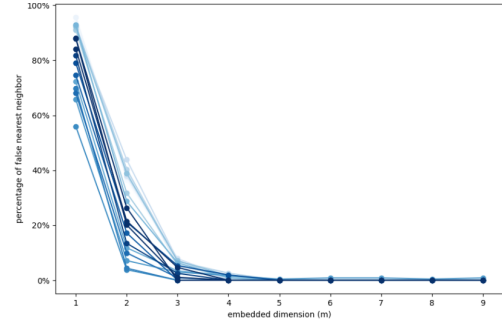


Figure 2. The percentage of false nearest neighbors with input data $x \equiv \text{APD}$ and lag $\tau = 1$. Each curve corresponds to a different τ_d value, varying from 0.42 (dark blue) to 0.401 (light blue). The percentage of false nearest neighbors decreases sharply as m increases, reaching near zero by $m = 4$.

$$\begin{aligned}I_{fi}(u, v) &= -vp(u - u_c)(1 - u) / \tau_d \\ I_{so}(u) &= u(1 - p) / \tau_0 + p / \tau_r \\ I_{si}(u, w) &= -w(1 + \tanh(k(u - u_c^{si}))) / (2\tau_{si})\end{aligned}\quad (17)$$

where:

$$\begin{aligned}\tau_v^-(u) &= q\tau_{v1}^- - q\tau_{v2}^- \\ p &= \mathcal{H}(u - u_c) \\ q &= \mathcal{H}(u - u_v)\end{aligned}\quad (18)$$

and $\mathcal{H}()$ is Heaviside step function

E. OVVR Model

The OVVR human model developed in 2011 by O'Hara et al.¹⁸ simulates the electrophysiological behavior of human ventricles and utilizes 41 differential equations per cell, representing 15 ionic currents and intracellular processes, enabling the study of complex cardiac phenomena such as action potential propagation and arrhythmias in the heart.

F. Current Identifiability Index (CII)

To further evaluate the role of individual ionic currents and their associated time constants τ_d , τ_0 , τ_r and τ_{si} , we applied the Current Identifiability Index³³ (CII). This index quantifies the sensitivity of the membrane potential and APD to perturbations of certain ionic currents. Since APD is the primary quantity from which LEs are computed in our analysis, the CII serves as an independent validation metric for assessing the physical significance of the LE results. That is, a current with a high identifiability index should exhibit a correspondingly sharp transition in the LE-based chaos quantification, while a current with low identifiability would be expected to exhibit a slow transition.

To this end, we apply the CII method to the 3V SIM model and examine the identifiability of its three major ionic currents. Our goal is to establish a qualitative correlation between the identifiability index and the transition sharpness observed in the LE results.

The ionic currents are organized into a data matrix A :

$$A = \begin{pmatrix} I_{fi}^1 & I_{so1}^1 & I_{so2}^1 & I_{si}^1 \\ \vdots & \vdots & \vdots & \vdots \\ I_{fi}^M & I_{so1}^M & I_{so2}^M & I_{si}^M \end{pmatrix}, \quad (19)$$

where I_j^k means current I for specific ion j at time step k ($t = k\Delta t$) and $A \in \mathbb{R}^{M,4}$ (M is the number of time steps). Notably, the slow outward current I_{so} from Eq. 17 is decomposed into two additive components, corresponding to the distinct time constants τ_0 and τ_r .

Then we do Singular Value Decomposition (SVD) process on the matrix so that:

$$A = U\Sigma V^T, \quad (20)$$

$$Av_i = \sigma_i u_i,$$

where v_i is the right singular vector and u_i is the left singular vector. Notice that Σ is a diagonal matrix and its

diagonal values are the singular values. Now, we know that:

$$\partial_t u(\mathbf{x}, t) \propto \Sigma I = A\mu, \quad (21)$$

$$\mu = (1 \cdots 1)^T$$

Now, consider a perturbed version on direction v_i , we have $A\bar{\mu}$, where $\bar{\mu} = \mu + \varepsilon v_i$.

Finally, the perturbed quantity should be:

$$\|A(\mu - \bar{\mu})\|^2 = (\varepsilon \sigma_i)^2 \quad (22)$$

So that a small value of singular value σ_i represents an insensitive perturbation direction v_i , which will all together form an insensitive space $S = \{v_i\}$, $\varepsilon_i < 0.5$ with threshold defined as 0.5. Then we calculate the projection P_j of unit vector for current j onto S and make $\text{CII}_j = 1 - P_j$. If $\text{CII}_j = 1$, then the unit vector for current j is completely outside of S and thus super sensitive, otherwise, if $\text{CII}_j = 0$, it is super insensitive.

III. DATA ACQUISITION

Voltage and action potential duration (APD) data from the 3V-SIM and OVVR models were simulated in 2D tissue using browser-based simulations. These simulations were implemented with WebGL via the Abubu.js library, which provides a simplified interface for GPU acceleration compared to traditional WebGL. This allows researchers without graphics programming experience to focus on the numerical and physiological aspects of the models. Abubu.js uses texture as the primary data structure, where each texture contains 512*512 pixels and every pixel has four channels: red (r), green (g), blue (b), alpha (α , transparency). In the 3V SIM model, only three channels (r, g, b) are used to store variables (u, v, w) and α is set to be 1.0. In the OVVR model, 11 separate textures are used, where each of them stores 4 state variables (41 state variables in total per cell).

When solving the PDEs, finite difference and forward Euler methods are applied respectively. The time and space discretizations are $dt = 0.1$ ms and $dx = dy = \frac{18}{512}$ cm, respectively. The boundary condition is using `GL_CLAMP_TO_EDGE` in WebGL, which means if the coordinates of pixels are $[0, 1]^2$, then any coordinate greater than 1.0 is set to 1.0, and any coordinate less than 0.0 is set to 0.0.

We conducted experiments across multiple parameter sets to quantify their complexity specially for spiral waves undergoing breakup. The same S1-S2 cross-field

protocol^{34,35} was used consistently across all configurations to initiate spiral activity. This protocol applies an initial planar stimulus (S1), followed by a well-timed localized second stimulus (S2), perpendicular to S1, during the refractory tail of the wavefront, facilitating the formation of spiral wave singularities, as shown in Fig. 3(A,B), allowing subsequent nonlinearity calculation.

We discarded an initial transient $T_i = 520000$ (approximately 1300 APDs) to ensure that the phase space trajectory settles onto one stable attractor or a group of attractors whose chaoticity we aim to quantify. This practice is consistent with common convention in cardiac simulations, where dynamics in the early stage are commonly excluded to eliminate transient behavior resulting from initialization. While all simulations were initiated using the same S1–S2 cross-field protocol, the resulting phase trajectories can differ across parameter sets due to their intrinsic dynamical properties. Discarding the transient ensures that the measured chaos reflects the long-term behavior of the attractor, not the initial evolution from stimulus onset. Following the transient, we collected data over a simulation window $\Delta T = 1310000$, which is long enough to capture the full geometry of the attractor and any potential transitions between distinct attractors. As shown in Fig. 3(C), APD signals were recorded every 10 dt (2 ms) at 25^2 evenly spaced spatial locations across the tissue.

Table I. Simulation configuration,

Parameter	Symbol	Value
Simulation time step	$d\tau$	0.1
Measurement time step	dt	4
Space step	dx, dy	$\frac{18}{512}$
Texture size	–	512×512
Measurement pixels	$\{k\}$	8×8
Transient time	T_i	520000
Measurement time	ΔT	[520000, 1830000]

IV. RESULT

A. Phase Space Reconstruction

The results are presented in three forms: (1) the reference standard results computed from full voltage data using the temporal method (temporal LE), (2) the APD-based estimate using the same temporal method (temporal LE), and (3) the APD-based estimate using the spatial-temporal method (spatial LE). The spatial-temporal algorithm evaluates one-step divergence, as defined in Eq. 10, which makes it unsuitable for voltage

signals that typically exhibit divergence over multiple steps (approximately one APD cycle). For this reason, the spatial-temporal method is not applied to the voltage data.

As noted earlier, a lag value of $\tau = 1$ is selected given that the simulation data is noise-free. The effect of the embedding dimension m on APD signals from the parameter set τ_d is shown in Fig. 2. A plateau is observed beyond $m = 4$, where the percentage of false nearest neighbors no longer decreases significantly. Therefore, we select $m = 4$ as the embedding dimension for all subsequent analyses. Similar plateaus are observed across other parameter sets. The maximum initial separation ϵ , used in both temporal and spatial LE calculations, is determined via a grid search.

B. 3V SIM Model

In the 3V-SIM model, modifying the gating constants of different ionic currents alters the biophysical behavior of cardiac cells, potentially leading to intercellular instability that amplifies the tissue’s nonlinear response. This cascade can result in increased LE, indicating a transition toward more chaotic dynamics. A key advantage of the 3V-SIM model is its ability to capture essential electrophysiological behavior using only three state variables per cell, while remaining flexible enough to represent species ranging from mice to humans. This makes it a valuable tool for investigating how ionic perturbations influence the degree of chaos across species. Since both single and multiple spiral waves are known to arise during life-threatening arrhythmias such as fibrillation, this study begins with characterizing single-spiral wave regimes and evaluates both spatial and temporal LEs to examine their correspondence with different spiral wave patterns.

1. Single Spiral Wave Pattern

According to the work by Fenton et al.⁵, various distinct single spiral wave patterns can be reproduced by tuning specific parameter sets in a simplified ionic model, as shown in Tab. II. These patterns range from simple circular spirals (Fig. 4A), drifting spirals (Fig. 4B–D), and more complex star-shaped structures (Fig. 4F). Interestingly, although many of these patterns exhibit visually similar tip trajectories or global wavefront dynamics, they display clearly distinct LE distributions depending on the estimation method applied. This underscores the necessity of evaluating both spatial and temporal aspects of instability when characterizing wave

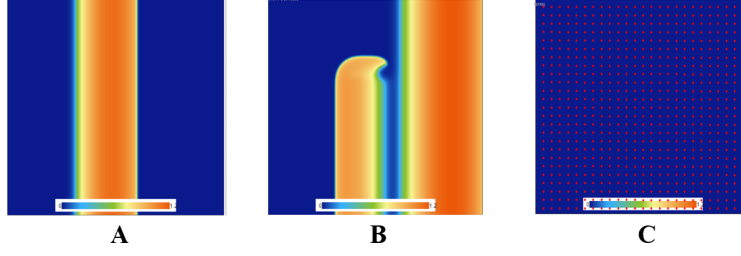


Figure 3. Initial condition: (A) Begin with voltage activation having a square shape from the left edge. (B) When the most left part of the square passes the middle of the map, another activation square in the middle bottom starts. (C) Red dots (25*25 dots in total) are the locations of data recorded.

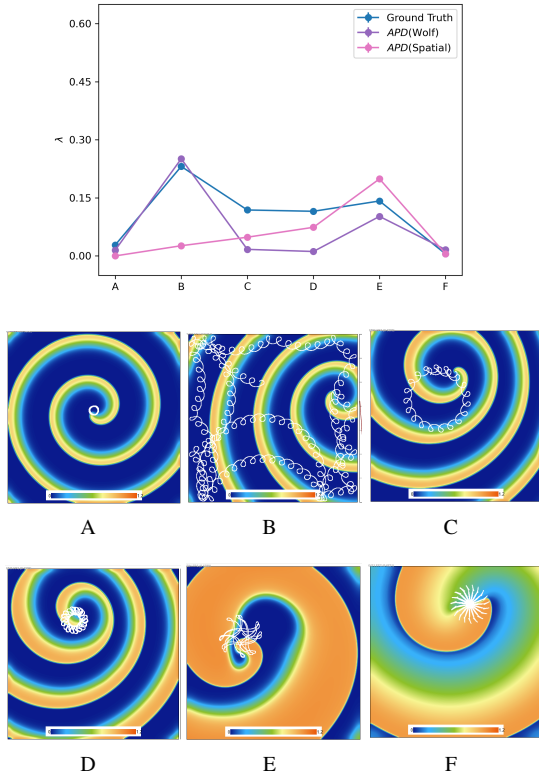


Figure 4. Top: LEs for different single spiral wave patterns. Bottom: Actual simulations of different spiral wave patterns. The white line represents the tip trajectory of the spiral wave.

dynamics in cardiac tissue.

In case B, the temporal LE is significantly higher than the spatial LE. This discrepancy likely arises from the random walking of the spiral core, as shown in the tip trajectory of Fig. 4B. From a spatial perspective, the overall pattern is a shifted version of a periodic spiral wave. However, when observed temporally, each cell without

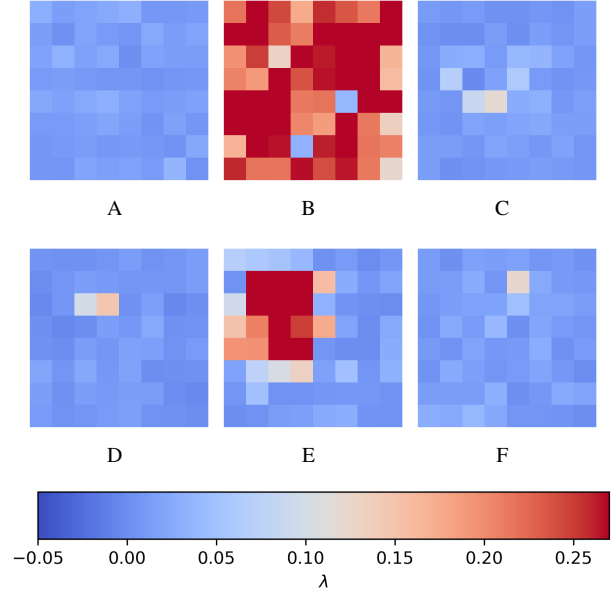


Figure 5. Heatmap for LE by APD(wolf).

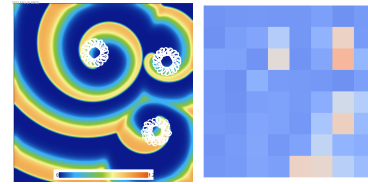


Figure 6. Left: Actual simulation frame in case D but with multi spiral waves. Right: The corresponding heat map. The LEs for this special case are respectively 0.16, 0.031, 0.11 for standard results from uvw, APD(wolf) and APD(spatial)

global spatial information undergoes a much more irregular and seemingly chaotic process. This mismatch between local and global dynamics results in a significant divergence between spatial and temporal LEs.

Table II. Detailed parameter values for spiral wave patterns A–F. Patterns A–E use Parameter Set 1 with varying τ_d ; Pattern F uses Set 2.

Parameter	A	B	C	D	E	F
τ_v^+	3.33	10
τ_{v1}^-	19.6	10
τ_{v2}^-	1000	10
τ_w^+	667
τ_w^-	11
τ_d	0.41	0.392	0.381	0.36	0.25	0.25
τ_0	8.3	10
τ_r	50	190
τ_{si}	45
k	10
V_c^{si}	0.85
V_c	0.13	0.13
V_v	0.055

By contrast, in cases A and F, both spatial and temporal LEs are nearly identical and close to zero, indicating globally periodic behavior. In case F, although the tip trajectory appears visually complex, it is exactly repeating, producing a strictly periodic spatial-temporal pattern. Similarly, in cases C–E, both LE measures are in closer agreement than in case B, though small discrepancies still appear. These are because that the spiral cores have larger radius compared to cases A and B, and their structure is more complex than that in case F. The increased complexity in their core shapes leads to slightly more chaotic behavior in the spatial LE. Meanwhile, since only a limited area near the core experiences irregularity, the averaged temporal LE remains smaller than the spatial LE.

This difference in these two methods is further supported by the temporal LE heatmaps in Fig. 5. In cases A and F, the maps are primarily blue, indicating low instability. In case B, red values are distributed more broadly, corresponding to the tip’s displacement across the domain. In cases C, D, and E, the red regions are localized around the spiral cores, reflecting the fact that only cells near the tip experience high temporal divergence. Notably, in case D, a pronounced red spot appears at the core, surrounded by blue regions elsewhere, highlighting the spatial localization of chaos captured by the temporal LE.

These results confirm that the two methods capture distinct aspects of spiral dynamics: the temporal LE highlights core displacement and local time-wise irregularity, while the spatial LE emphasizes geometric complexity in the wave structure. When both core position and shape are stable, as in A and F, both estimators con-

verge toward zero. When either aspect becomes unstable, the difference between methods provides insight into the underlying source of chaos. When both position and shape are unstable, we could see consistency between these two methods as well, indicating spatial-temporal chaos.

2. Multiple Spiral Wave Pattern

The critical transition occurs when certain identifiable parameters vary within specific ranges. Here, we pick the gate variables $\{\tau_d, \tau_0, \tau_r, \tau_{si}\}$ for currents $\{I_{fi}, I_{so}, I_{si}\}$ and try to find the sensitive range to pinpoint the transition spot. Tab. III lists the parameter values, with the ones highlighted in red indicating those subject to tuning. The range is carefully selected to elucidate the transition state.

Table III. Parameter settings for the 3V-SIM model. Red indicates tuned parameters.

Parameter	Value	Tuned Range
C_m	1	—
τ_v^+	3.3	—
τ_{v1}	16	—
τ_{v2}	5	—
τ_w^+	350	—
τ_w^-	80	—
τ_d	0.41	[0.406, 0.411]
τ_0	9	[7.2, 9.4]
τ_r	34	[33.5, 34.5]
τ_{si}	27	[26.45, 26.95]
k	15	—
u_c^{si}	0.45	—
u_c	0.15	—
u_v	0.04	—

In Figure 7, we try to investigate the nonlinear property of τ_d , which controls the capacity of the gate of I_{fi} or Na^+ current, as shown in Eq. 17. We present the results for varying τ_d from 0.4050 to 0.4115, comparing APD-based LEs with standard uvw results. Three dynamic regimes are identified—A (chaotic), B (transition), and C (periodic). This different nonlinear property can also be seen in the actual simulation frames, where A exhibits frequent spiral wave breakups and C shows stable, self-repeating spiral activity. B displays mixed behavior, with B1 (chaotic) and B2 (quasiperiodic), highlighting its transitional nature. The restitution plots (APD vs. DI) further support this classification,

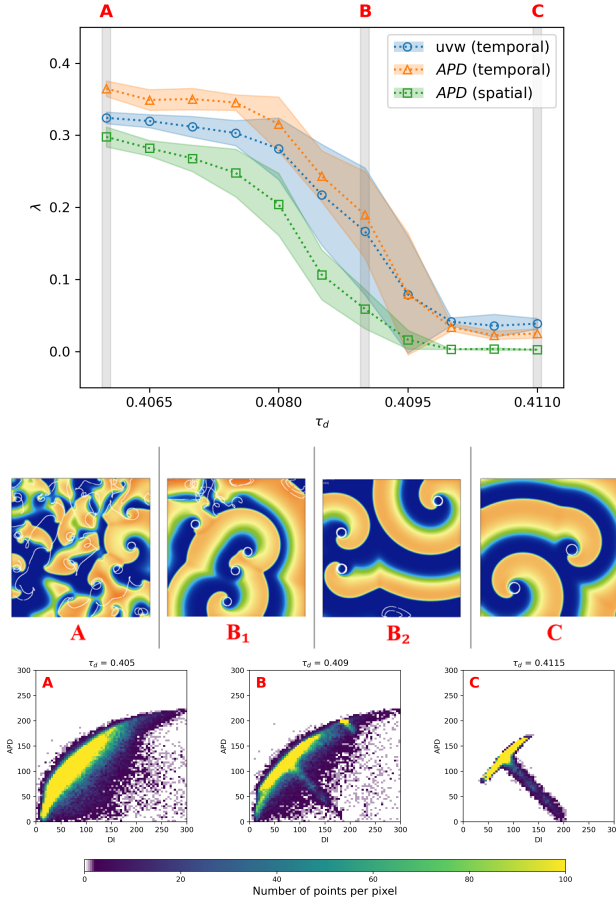


Figure 7. Top: LEs for τ_d where A, B, C represents different τ_d state. Middle: Actual simulations of different τ_d states. The white line represents the tip trajectory of the spiral wave. B₁ and B₂ represent two possibilities that the B state could become. Bottom: Restitution curves of different τ_d states. State A stays chaotic, state B stays either less chaotic or quasiperiodic, and state C stays only periodic.

showing a broader APD distribution in chaotic states and a narrower spread in periodic states. These observations collectively demonstrate a clear transition from chaos to periodicity. Notably, the APD-based LE results closely align with those derived from full-state data, confirming that APD preserves the system's underlying nonlinear dynamics.

Similarly, Fig. 8 presents the results for the τ_r dataset. Notably, the transition state happening at B exhibits a dynamic behavior similar to that observed in the τ_d dataset. The system oscillates between periodic and quasiperiodic states, with quasiperiodic state showing more wave breakups. These breakups are visually manifested as white tip trajectories forming line-like patterns. Further-

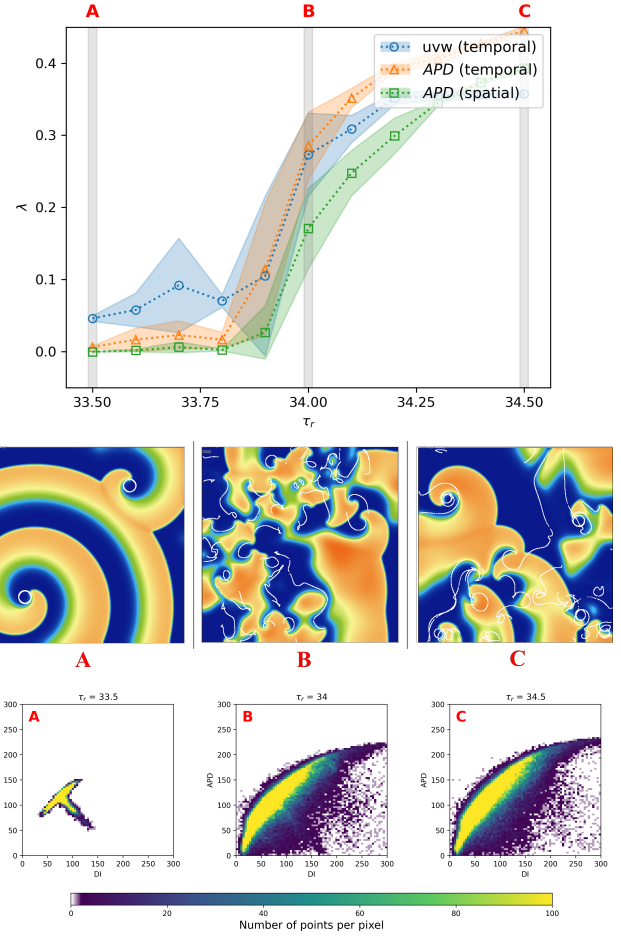


Figure 8. Top: LEs for τ_r where A, B represents different τ_r state. Middle: Actual simulations of different τ_r states. The white line represents the tip trajectory of the spiral wave. B₁ and B₂ represent two possibilities that the B state could become. Bottom: Restitution curves of different τ_r states.

more, the restitution curves corresponding to both transition states reveal comparable profiles, reinforcing the presence of a shared underlying bifurcation mechanism.

In contrast, the τ_0 dataset shown in Fig. 9 demonstrates a significantly reduced change rate of the LE. The transition window spans a wider range at approximately [7, 9.5], which differs by several orders of magnitude compared to the sharp transitions observed in τ_d and τ_r . This suggests that τ_0 plays a more stabilizing role, yielding a slower and smoother progression from chaos to period.

Lastly, Fig. 10 illustrates the behavior under variations of τ_{si} . Once again, a similar transition state B emerges where quasiperiodic and periodic behaviors overlap. Additionally, the directionality of LE change appears parameter-dependent. For positively signed pa-

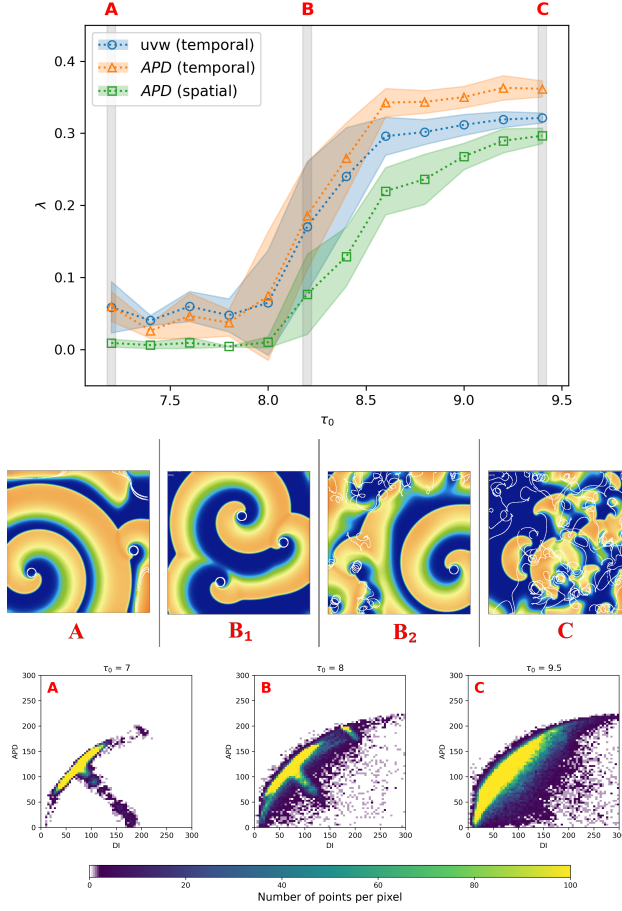


Figure 9. Top: LEs for τ_0 where A, B represents different τ_0 state. Middle: Actual simulations of different τ_0 states. The white line represents the tip trajectory of the spiral wave. B₁ and B₂ represent two possibilities that the B state could become. Bottom: Restitution curves of different τ_0 states.

parameters such as τ_0 and τ_r , an increase tends to widen the spiral wave, which then requires a larger domain to maintain wave coherence. That is to say, when constrained to a fixed spatial domain, this leads to more frequent wave collisions and breakups, indicating a higher LE and stronger chaos. This trend reinforces the notion that parameter-induced geometric alterations in spiral waves are central to chaos modulation.

A clear correlation emerges between the geometric behavior of spiral cores and the corresponding LE. In periodic state, the spiral core typically traces a stable, circular path, as observed in state C for τ_d and τ_{si} and in state A for τ_0 and τ_r . In contrast, the chaotic states are characterized by irregular, non-repeating core trajectories caused by more frequent wave breakups. This pro-

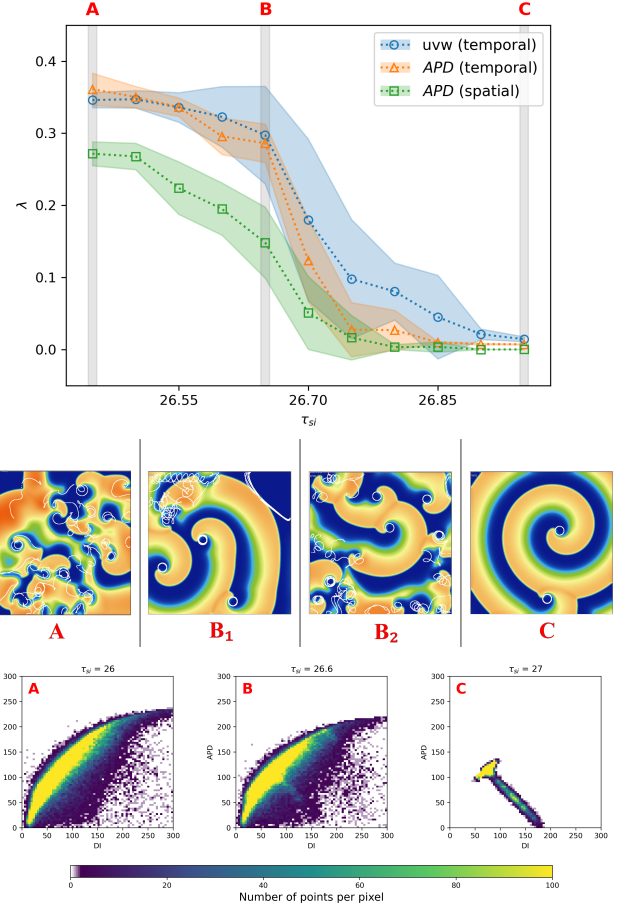


Figure 10. Top: LEs for τ_{si} where A, B represents different τ_{si} state. Middle: Actual simulations of different τ_{si} states. The white line represents the tip trajectory of the spiral wave. B₁ and B₂ represent two possibilities that the B state could become. Bottom: Restitution curves of different τ_{si} states.

gression from fragmented to coherent spiral dynamics mirrors the transition from high to low LEs. Such geometric transitions suggest the potential for developing image-based chaos classification methods. In particular, convolutional neural networks (CNNs), commonly used for pattern recognition, may be employed to learn and classify levels of chaoticity based on spatial features of spiral core evolution.

To assess temporal variability, each post-transient simulation was divided into five equal-duration segments, and the LE was computed independently for each. The standard deviation of these values, shown as the shaded region, reflects the coexistence of different dominant attractors whose LE values differ within a relatively confined range. Across all parameter sets, the transition

Gate	Current	CII	Sensitivity
τ_d	I_{fi}	1.0	Super sensitive
τ_0	I_{so1}	1.1e-16	Insensitive
τ_r	I_{so2}	0.76	Sensitive
τ_{si}	I_{si}	0.65	Sensitive

Table IV. CII for different current gates.

state B consistently exhibits elevated standard deviation. This reflects the presence of multiple coexisting attractors—chaotic, quasiperiodic, and periodic attractors. As a result, even with the same initial condition and after the transient period, the system can still fall into different attractors, leading to divergent behaviors and thus a wide range of LEs. This sensitivity further supports the interpretation of the transition regime as a dynamically unstable region.

3. CII and the sharpness of transition region

We used data from state B in Fig. 7 the CII. The data used are shown in Fig. 11. After SVD, we get $U\Sigma V^T$ according to Eq. 20 and the right singular matrix:

$$V = \begin{bmatrix} -0.45 & -1.11e-16 & 0.69 & -0.57 \\ 0.89 & 0.00 & 0.33 & -0.30 \\ 0.02 & 8.60e-16 & 0.65 & 0.76 \\ 0.00 & 1.00 & -6.66e-16 & -6.66e-16 \end{bmatrix}$$

with corresponding singular values $\sigma = \{4.42, 3.42, 0.72, 0.40\}$. As mentioned earlier, we considered $\sigma < 0.5$ as insensitive directions and thus did a qualitative analysis of the insensitive space S. Then after calculations of projections onto S by different current gates, we get the CII as below:

Now if we take transition width range order of 0.01 as super sensitive, 0.1 as sensitive and ≥ 1 as insensitive, we could see that the CII qualitatively describe the sensitivity of the transition region showed in LE results.

C. OVVR Model

Compared to the 3V-SIM model, the OVVR model exhibits higher physiological complexity, with 41 state variables per cell and 15 ionic currents governing the action potential dynamics. This higher dimensionality increases the system's sensitivity to small perturbations, which is reflected in larger standard deviations of LEs and more frequent transitions between coexisting attractors.

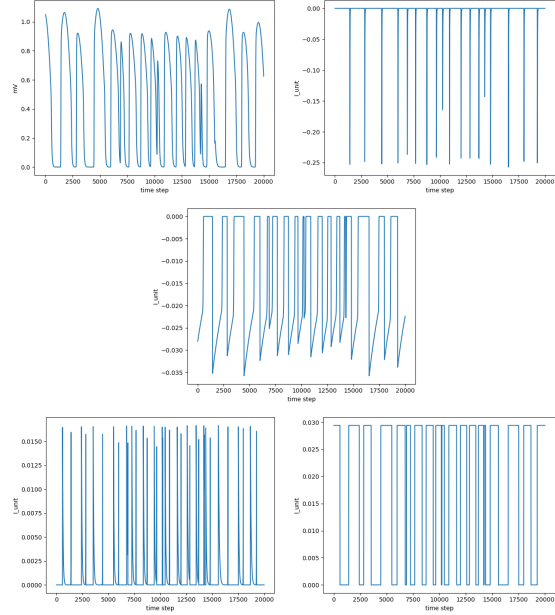


Figure 11. The data used in ICC calculations. Top Left: the voltage u . Top Right: Current I_{fi} . Middle: Current I_{si} . Bottom Left: Current I_{so1} . Bottom Right: Current I_{so2} .

In the simulations, the L-type calcium conductance scaling factor (C_{CaL}) was varied over the range $[0.86, 1.04]$, while all other parameters were default values as described in O'Hara et al.¹⁸. At the lowest C_{CaL} value, the tissue maintained one or two stable spirals with low LEs. The standard deviation remained quite small for both temporal and spatial estimates, indicating that a single periodic attractor dominated the dynamics.

As C_{CaL} increased, the action potential plateau shortened, promoting earlier wavefront collisions and occasional spiral breakup. These changes led to higher LEs and their standard deviations, signaling the emergence of multiple coexisting attractors. In this range, a single system under small perturbations could fall into different attractors, producing a range of LEs.

At the upper end of C_{CaL} , the model entered a fully developed spatiotemporal chaotic state, with frequent multi-spiral breakups (state C in Fig. 12). Unlike the 3V-SIM case, where spatial LEs stayed below temporal ones, here the spatial measures were larger, suggesting more intense spatial chaos. The temporal LE curves displayed a broad shaded region, indicating the model's greater dimensionality. In contrast, the spatial LE curves showed a narrower shaded region, suggesting their potential for quantifying chaotic states in high-dimensional systems.

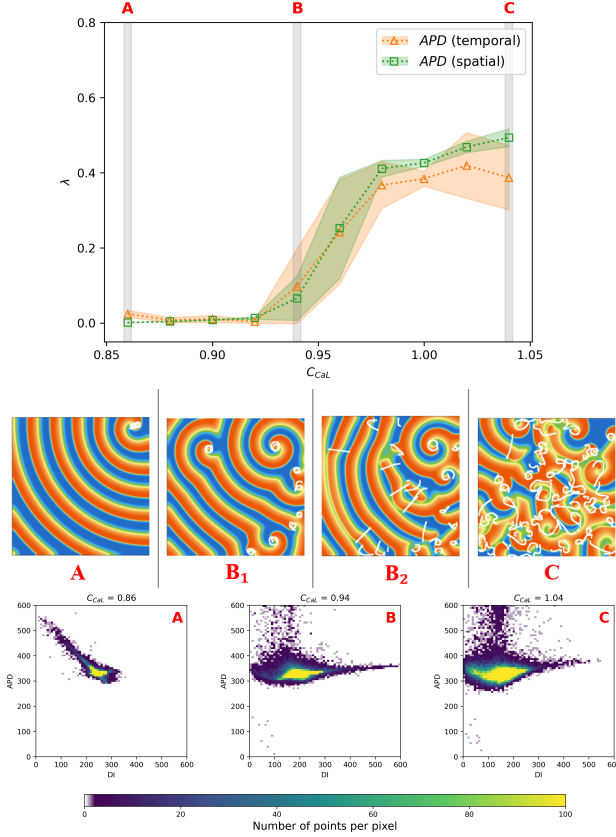


Figure 12. Top: LEs for C_{CaL} where A, B represents different C_{CaL} state. Middle: Actual simulations of different C_{CaL} states. The white line represents the tip trajectory of the spiral wave. B₁ and B₂ represent two possibilities that the B state could become. Bottom: Restitution curves of different C_{CaL} states.

D. Effect of Data Quality on LE Estimation Accuracy

Prior studies have emphasized that limited spatial or temporal resolution could potentially obscure important features of spiral wave dynamics, leading to mischaracterization of underlying instability³⁶. In light of this, we conducted a series of tests varying both the number of spatial points and the temporal length of APD recordings to examine how data quality affects the accuracy and reliability of LE estimation, and to determine the minimal data requirements for robust chaos quantification.

Figure 13 shows the relationship between root mean square error (RMSE) and the number of spatial points used for both APD-based methods. For the temporal APD method, we observe a clear decline in RMSE as more spatial points are included, indicating improved robustness and gradual convergence. In contrast, the spatial APD method exhibits a relatively stable RMSE

plateau, showing little sensitivity to the number of points used. However, after convergence, the temporal method achieves a lower RMSE than the spatial method.

This difference likely arises from the underlying design of the algorithms. The spatial method, defined in Eq. 11, captures temporal divergence over a single step while placing greater emphasis on spatial chaos by memorizing all the spatial $\langle k, h \rangle$ pairs, as shown in Eq. 9. Based on this formulation, one would expect a large number of spatial points to capture spatial complexity and achieve convergence. However, the results suggest that only a few points are sufficient for stable estimates. This may be due to the nature of the 3V-SIM Model, which exhibits strong spatiotemporal chaos. In such scenarios, spatial and temporal variations contribute almost equally to the overall chaos; thus, the averaging in Eq. 11 treats them symmetrically. As a result, longer APD sequences could offset the lack of spatial sampling, maintaining stability in the spatial LE estimates despite fewer points.

Figure 14 illustrates the effect of varying APD sequence length. As expected, the temporal method benefits greatly from longer sequences, consistent with its role in capturing long-term divergence behavior. The spatial method, however, again shows minimal dependence on sequence length due to its one-step formulation. While this robustness allows it to calculate with shorter time series, the resulting precision saturates at an RMSE around 0.06.

These experiments reveal a trade-off between the two methods. The temporal approach is data-intensive but capable of higher precision when adequate input is available. The spatial method is more data-efficient and performs surprisingly well in spatiotemporally chaotic regimes, where long APD sequences help compensate for reduced spatial information. However, in cases dominated by purely spatial or purely temporal chaos, spatial method may require more samplings to converge.

This distinction is particularly relevant for experimental applications where spatial resolution or temporal duration is limited. Depending on the constraints, one can prioritize the method that balances accuracy with available data.

V. DISCUSSION AND CONCLUSION

We introduced and evaluated two APD-based methods for estimating LE to characterize spatiotemporal chaos in cardiac tissue models. Both approaches operate on reconstructed data from APD and rely on lag embedding to recover underlying dynamics. The temporal method emphasizes long-range divergence, using spatial information for averaging. The spatial method, on the other

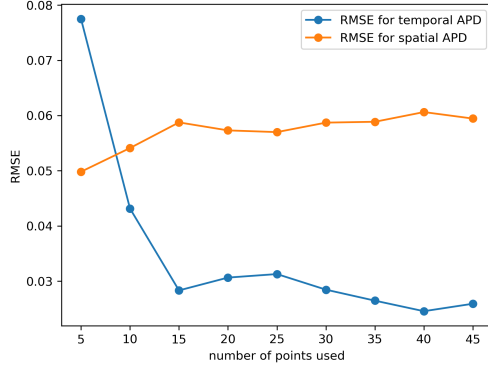


Figure 13. RMSE of LE estimation versus number of points used. Temporal LE improves with more samples, while spatial LE remains relatively stable.

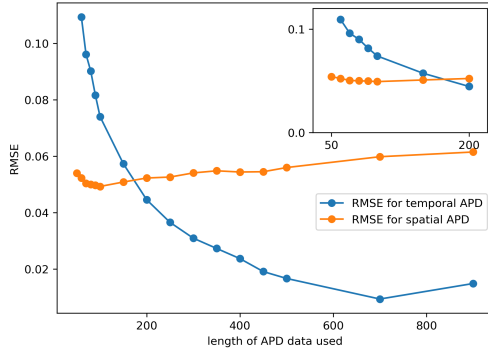


Figure 14. RMSE of LE estimation versus APD sequence length. Temporal LE benefits from longer sequences; spatial LE shows little dependence.

hand, evaluates one-step divergence between neighboring spatial points at each time frame, with temporal length contributing to statistical averaging. Together, they provide complementary ways to assess dynamical instability from reduced data.

To assess performance, we compared these methods against the ground-truth method by utilizing full state variables locally with Wolf’s algorithm. We have conducted comparisons on single spirals and multiple spirals cases and both algorithms perform decent precision in LE estimations.

We examined how the two methods reflect the structure of spiral wave patterns. In relatively stationary single-spiral cases—such as cases A, E, and F in Fig. 4, both temporal and spatial LE estimates align well with reference values, confirming their ability to capture periodic dynamics or low-dimensional chaos. In cases with meandering or drifting cores (e.g., cases B–D in Fig. 4 and D2 in Fig. 6), the methods diverge in their

results: the temporal LE detects chaos when spiral cores undergo displacement, indicating temporal instability at the pixel level, while the spatial LE is more sensitive to the geometric irregularity of the spiral shape itself. This is particularly evident in case D2, where the spiral cores remain stationary but exhibit distorted, non-periodic shapes, resulting in a periodic signal under the temporal method but a chaotic signature under the spatial method. A similar pattern appears in Fig. 5, where red regions in the temporal LE map correspond to drifting cores (e.g., B and E), while spatial irregularity without displacement leads to predominantly blue (periodic) signals in the temporal map, despite the spatial LE indicating local instability.

In more disordered multi-spiral regimes, we investigated how tissue instability responds to ionic perturbations by systematically varying parameters associated with gating variables in both the 3V-SIM and OVVR models. Across different tuning directions, both APD-based LE estimators revealed clear sensitivity to gating kinetics, with changes in certain parameters either increasing or decreasing the chaos. These outcomes reflect how specific ionic time constants modulate recovery dynamics and, in turn, influence the prevalence of wavebreaks and reentrant activity. This supports the broader view that spatiotemporal complexity in excitable media is tightly linked to the interplay between recovery properties and wavefront propagation.

As additional support for the validity of our LE-based chaos estimation, we compared the trend of LE growth to the behavior of the CII across parameter variations. We observed that the slope of the CII curve for each ionic current qualitatively aligns with the slope of the corresponding LE curve. While the two measures are not numerically proportional, this correspondence reinforces the idea that our LE calculations capture physiologically meaningful instability. Moreover, the CII analysis offers additional insight into the structure of the 3V-SIM model by indicating which currents exhibit greater sensitivity to perturbations and how that sensitivity evolves alongside the onset of chaotic dynamics.

Finally, we analyzed the sensitivity of both methods to data quality by varying spatial sampling density and APD sequence length. The temporal method exhibits clear dependence on both factors. A larger number of spatial points is required to ensure robustness, while longer sequences enhance convergence due to the method’s reliance on long-term divergence computation. The spatial method, however, converges quickly even with sparse data, and remains stable across different APD lengths. This efficiency makes it attractive for experimental applications with limited spatial resolution or short recording windows.

In summary, the temporal method offers higher accu-

racy and better sensitivity to dynamic transitions but requires more data. The spatial method is computationally efficient, robust to limited sampling, and performs reliably in regimes with strong spatiotemporal coupling. Together, these methods provide a practical toolkit for assessing chaos in cardiac systems using accessible observables.

Future work could apply this framework to optical mapping or clinical data, extend the APD-based estimation to three-dimensional simulations, or integrate the LE features into machine learning pipelines for arrhythmia prediction. Moreover, the spatial patterns revealed by LE distributions may serve as indicators of vulnerable regions in the tissue, supporting classification and control strategies in arrhythmia management.

CODE AND DATA AVAILABILITY

The complete simulation and analysis code, including all WebGL applications and pre-calculated data, is publicly available at [GitHub](#).

ACKNOWLEDGEMENTS

We thank [names of colleagues] for valuable discussions and [any lab members] for technical assistance. This work was supported by [funding agency and grant number if applicable]. Computations were performed using resources provided by [institution0].

REFERENCES

- ¹M. K. Mulimani, S. Zimik, J. K. Alageshan, and R. Pandit, [Communications in Nonlinear Science and Numerical Simulation](#) **126**, 107428 (2023).
- ²A. Molavi Tabrizi, A. Mesgarnejad, M. Bazzi, S. Luther, J. Christoph, and A. Karma, [Physical Review X](#) **12**, 021052 (2022).
- ³A. Loppini, A. Gizzi, R. Ruiz-Baier, C. Cherubini, F. H. Fenton, and S. Filippi, [Physical Review E](#) **98**, 062405 (2018).
- ⁴F. Fenton and A. Karma, *Chaos: An Interdisciplinary Journal of Nonlinear Science* **8**, 20 (1998).
- ⁵F. H. Fenton, E. M. Cherry, H. M. Hastings, and S. J. Evans, *Chaos: An Interdisciplinary Journal of Nonlinear Science* **12**, 852 (2002).
- ⁶A. Garfinkel, Y. Kim, O. Voroshilovsky, Z. Qu, J. Kil, M. Lee, H. Karagueuzian, J. Weiss, and P. Chen, *Journal of Clinical Investigation* **99**, 305 (1997).
- ⁷R. A. Gray, A. M. Pertsov, and J. Jalife, *Science* **280**, 60 (1998).
- ⁸T. Shajahan, S. Sinha, and R. Pandit, *Physical Review E* **73**, 036205 (2006).
- ⁹J. N. Weiss, A. Karma, Y. Shiferaw, P.-S. Chen, A. Garfinkel, and Z. Qu, *Circulation research* **98**, 1244 (2006).
- ¹⁰J. Jalife, *Journal of Cardiovascular Electrophysiology* **14**, 776 (2000).
- ¹¹M. T. Rosenstein, J. J. Collins, and C. J. De Luca, *Physica D: Nonlinear Phenomena* **65**, 117 (1993).
- ¹²A. Wolf, J. B. Swift, H. L. Swinney, and J. A. Vastano, *Physica D: nonlinear phenomena* **16**, 285 (1985).
- ¹³I. Hagerman, H. Bergman, B. Eklund, O. Ohlsson, and O. Andersson, *Cardiovasc. Res.* **31**, 410 (1996).
- ¹⁴A. Casaleggio and S. Braiotto, *Chaos Solitons Fractals* **8**, 1591 (1997).
- ¹⁵G. Valenza, L. Citi, A. Lanatà, E. P. Scilingo, and R. Barbieri, *Front. Neuroeng.* **5**, 3 (2012).
- ¹⁶A. N. Pavlov, O. N. Pavlova, O. V. Sosnovtseva, E. Mosekilde, and N.-H. Holstein-Rathlou, in *Proc. SPIE*, Vol. 4396 (2000) pp. 272–279.
- ¹⁷R. V. Solé and J. Bascompte, *Journal of Theoretical Biology* **175**, 139 (1995).
- ¹⁸T. O'Hara, L. Virág, A. Varró, and Y. Rudy, *PLoS computational biology* **7**, e1002061 (2011).
- ¹⁹P. Grassberger and I. Procaccia, *Physical review letters* **50**, 346 (1983).
- ²⁰F. Takens, in *Dynamical Systems and Turbulence, Warwick 1980: proceedings of a symposium held at the University of Warwick 1979/80* (Springer, 2006) pp. 366–381.
- ²¹A. Wolf *et al.*, *Chaos* **16**, 285 (1986).
- ²²H. Kantz and T. Schreiber, *Nonlinear time series analysis* (Cambridge university press, 2003).
- ²³T. Sauer, J. A. Yorke, and M. Casdagli, *Journal of statistical Physics* **65**, 579 (1991).
- ²⁴G. Sugihara, R. May, H. Ye, C.-h. Hsieh, E. Deyle, M. Fogarty, and S. Munch, *science* **338**, 496 (2012).
- ²⁵M. B. Kennel, R. Brown, and H. D. Abarbanel, *Physical review A* **45**, 3403 (1992).
- ²⁶X. Jiang and H. Adeli, *Integrated Computer-Aided Engineering* **10**, 287 (2003).
- ²⁷T. Buzug and G. Pfister, *Physical review A* **45**, 7073 (1992).
- ²⁸J. Theiler, *JOSA a* **7**, 1055 (1990).
- ²⁹E. M. Cherry and F. H. Fenton, *American journal of physiology-Heart and circulatory physiology* **286**, H2332 (2004).
- ³⁰E. Cherry, F. Fenton, *et al.*, *J Theor Biol* **253** (3): 544–60 (2008).
- ³¹M. Courtemanche and A. T. Winfree, *International Journal of Bifurcation and Chaos* **1**, 431 (1991).
- ³²C.-h. Luo and Y. Rudy, *Circulation research* **68**, 1501 (1991).
- ³³K. H. Jørgen, S. Wall, and A. Tveito, *Chaos* **29**, 073102 (2019).
- ³⁴A. Smith and B. Doe, *Front. Physiol.* **11**, 1234 (2020).
- ³⁵C. Jones and D. Roe, *PNAS* **115**, 20237–20242 (2018).
- ³⁶E. M. Cherry and F. H. Fenton, [Chaos: An Interdisciplinary Journal of Nonlinear Science](#) **18**, 013105 (2008).